Theoretical characterization of annular array as a volumetric optoacoustic ultrasound handheld probe

Mohammad Azizian Kalkhoran
Didier Vray

SPIE.

Theoretical characterization of annular array as a volumetric optoacoustic ultrasound handheld probe

Mohammad Azizian Kalkhoran* and Didier Vray
Université de Lyon, Université Claude Bernard Lyon 1, CREATIS, CNRS UMR5220, Inserm U1044, INSA-Lyon, Lyon, France

Abstract. Optoacoustic ultrasound (OPUS) is a promising hybridized technique for simultaneous acquisition of functional and morphological data. The optical specificity of optoacoustic leverages the diagnostic aptitude of ultrasonography beyond anatomy. However, this integration has been rarely practiced for volumetric imaging. The challenge lies in the effective imaging probes that preserve the functionality of both modalities. The potentials of a sparse annular array for volumetric OPUS imaging are theoretically investigated. In order to evaluate and optimize the performance characteristics of the probe, series of analysis in the framework of system model matrix was carried out. The two criteria of voxel crosstalk and eigenanalysis have been employed to unveil information about the spatial sensitivity, aliasing, and number of definable spatial frequency components. Based on these benchmarks, the optimal parameters for volumetric handheld probe are determined. In particular, the number, size, and the arrangement of the elements and overall aperture dimension were investigated. The result of the numerical simulation suggests that the segmented-annular array of 128 negatively focused elements with $1\lambda \times 20\lambda$ size, operating at 5-MHz central frequency showcases a good agreement with the physical requirement of both imaging systems. We hypothesize that these features enable a high-throughput volumetric passive/active ultrasonic imaging system with great potential for clinical applications. © *2018 Society of Photo-Optical Instrumentation Engineers (SPIE)* [DOI: 10.1117/1.JBO.23.2.025004]

Keywords: optoacoustic imaging; ultrasound imaging; photoacoustics; volumetric imaging; handheld probe; sparse array.

Paper 170659R received Oct. 9, 2017; accepted for publication Jan. 25, 2018; published online Feb. 27, 2018.

1 Introduction

Arguably, clinical diagnoses are becoming more reliant on the competence of imaging systems in visualization of the anatomy and physiology. The distinguishing characteristic of an imaging modality is greatly defined by its mechanism of contrast.[1] In this respect, medical ultrasound (US) is subjected to the mechanical impedance mismatches of the investigating media. Although it is sufficient to display the anatomy, pathological situations require far more dynamic contrast. Optoacoustic (OA) imaging benefits from the optical selective absorption associated with the chromophoric molecules and affords manifold contrasts. Through the OA effect, characteristics of absorbing structures are encoded in a broadband acoustic waves. OA can be considered as a passive acoustic imaging in a sense that the acoustic waves are induced inside the tissue. Hence, by employing the array of ultrasonic sensors, combination of OA and US is inherent and worthwhile. The unrivalled advantage of optoacoustic/ultrasound (OPUS) stems from the precise coregistration and correspondingly, the correlation between the detailed anatomical data of ultrasound and physiological information of OA images.

Effectively, ultrasound (US) probes paved the way for various clinical and preclinical applications of OPUS.[2–4] Despite the advantages, employed probes are essentially optimized for ultrasound imaging. For example, an aperture as large as 60λ would suffice for 1 deg spatial resolution,[5] whereas in the backward epi-OA imaging systems, the detection view angle of less than 2π results in inaccurate estimation.[6,7] Using speckle illumination technique, in Ref. 8, the angular view is increased by confining the boundary of optically excited acoustic sources, albeit at the cost of imaging depth. Analogously, ultrasonic thermal encoding[9] has been practiced by extending the idea of nonuniform signal generation for deeper regions. However, the acquisition time for these methods is far from the real-time imaging. In an alternative approach, the effective detecting aperture has been increased virtually via coupling the acoustic reflectors.[10,11] Although the success of this approach is practically demonstrated, the required geometry restricts the clinical applications.

Aside from the partial view angle, volumetric imaging is faced with multifold challenges. Given the $\lambda/2$ interelement spacing constraint (to avoid grating lobes), 60λ aperture requires high transducer (element) counts and expensive hardware.[12] To cope with, variety of undersampling strategies have been pursued,[13–16] among them, aperiodic sparse arrays are offering 60λ aperture size with maximum 256 elements.[5,17,18] In order to optimize the ultrasonic pulse echo beam quality and signal-to-noise ratio (SNR), the density of elements is tapered toward the center of aperture.[5,19] Consequently, the efficient integration with light delivery system for OA imaging is not trivial. Reference 20 discusses the optimum trade-off among the illumination, aperture angle of view, SNR, number, and size of the elements for a universal handheld probe. The imaging system seems impeccable for volumetric OA imaging, but the focused arrangement of the integrated staring transducers may not proffer the field of view (FOV), SNR, or the contrast expected from classical ultrasound systems.[21]

*Address all correspondence to: Mohammad Azizian Kalkhoran, E-mail: mohammad.azizian-kalkhoran@insa-lyon.fr

The potentials of planar annular array in terms of achievable resolution and uniform sensitivity for three-dimensional (3-D) OPUS imaging have been theoretically demonstrated.[22–24] Yet for the otherwise point such as transducers, the directional response, and averaging over the surface of the elements deteriorate the imaging performance. While the averaging behavior increases the SNR, the ill-suited directional response can be treated by negative acoustic lens.[25] Withal, in such configurations there is not much degree of freedom to simultaneously evaluate the effect of number and size of the elements. In a comparative study, similar performance between sunflower Fermat-spiral array and circular-annular array has been found (see Ref. 18). The lesser periodicity in Fermat spiral configuration encourages the sparser distribution and subsequently more freedom in the choice of parameters. The sparer array also means a larger aperture, which leads to a larger view angle, more angular frequency, and simply more spatial degree of freedom in defining the true object.[26] However, a pervasive analysis framework is required to provide an insight to the imaging performance of the designed system and proceed with further optimization. A common objective assessment technique for imaging systems is based on the point spread function (PSF) and spatial sensitivity.[26–28] Often considered as the system response to a point source, PSF is highly biased to the merits of the reconstruction algorithm. Alternatively, PSF can be calculated analytically via a linear model based on the spatial impulse response[29] that incorporates the properties of transceivers. For assessment of a shift variant system such as OPUS, reliable source localization in terms of standalone contribution and resolvability from the neighboring is crucial.

In this work, we are investigating the effect of the size, number, and arrangement of negatively focused transducers in annular array for a multipurpose 3-D OPUS handheld probe. The proposed geometry has the advantage of mitigating the transducer/channel counts required for 3-D imaging while preserving the spatial resolution and uniform insonification for the FoV.[22,23] The inherent central cavity of the probe furnishes the in-line illumination, which is expedient for maximizing the fluence.[30] In the next section, we explain the theoretical development of a linear model that comprises the behavior of an imaging system. Two evaluation methods, namely voxel crosstalk matrix[28] and eigenanalysis, have been briefly introduced and their ability in interrogating the model and correspondingly assessing the characteristics of the imaging system is discussed. The former provides information w.r.t. the system sensitivity and spatial aliasing while the latter addresses the quantity and quality of spatial frequency components. The assessment is followed by the system optimization with regards to the number, size, and geometry of the detecting aperture, and the results are shown in Sec. 3. Finally, in Sec. 4 the optimal choice of parameters, concluding remarks, and future directions are discussed.

2 Methods

2.1 Construction of the Model

Acoustic imaging is concerned with interpreting the detected induced or scattered waves from the surface of medium. In linear regime, the governing equation for a homogeneous medium satisfies[31]

$$\frac{\partial^2 p(r,t)}{\partial t^2} - \nu^2 \nabla^2 p(r,t) = s(r,t), \qquad (1)$$

where p is the diverging acoustic wave from the source s with the speed of sound ν related to the medium. The source represents the reflectivity R for the insonified scatterers[32] (Eq. 2) or the capability of the illuminated absorbers to transform photons energy to acoustic wave. The latter is characterized by the product of absorption coefficient μ_a of the chromophores, temperature-dependent Grüneisen parameter Γ representing the thermoelastic efficiency of the chromophores and optical fluence $\phi(r)$ (Eq. 3).

$$s_{US}(x,y,z) = [u_{exc}(t) * h_{tr}^{IR}(t)]R(x,y,z), \qquad (2)$$

$$s_{OA}(x,y,z) = \mu_a(x,y,z)\Gamma(x,y,z)\phi(x,y,z), \qquad (3)$$

where $u_{exc}(t)$ is the excitation pulse, $*$ represents the convolution in time, and h_{tr}^{IR} the transmit impulse response of the transducer. The projection of the source on the transducer surface is recorded in the form of RF signal u_{rec}. This spatiotemporal sensing behavior of the transducers is given by the transfer function (Fig. 1) and is composed of two parts: I. The spatial filtering dictated by the transducer geometry, which is attributed to the averaging effect (integral part in Eq. 4) and is formulated by the spatial impulse response $[h^{SIR}(r,t)]$. II. The temporal band-pass filtering, which is imposed by the acoustoelectrical impulse response $[h^{AIR}(t)]$ of the transducer. Hence, the recorded pressure field by the active area of the transducer A_d can be expressed via Huygens' principle[33]

$$u_{rec}(r,t) = h_{re}^{AIR}(t) * W \frac{\partial}{\partial t}\left\{ \int_{A_d} \frac{\delta[t - (|r_s - r_{re}|)/\nu]}{|r_s - r_{re}|} dA_d \right\}, \qquad (4)$$

where r_s and r_{re} represent the source and receiving element distance from the control point, and W denotes an adaptive weighting factor, which conforms to the nature of the source. For US, it can be considered as the tissue acoustic attenuating properties, whereas in OA, the deposited optical energy in the volume of interest. Therefore, the recorded projection u_{rec} of any discrete point within the aperture FoV can be formulated as
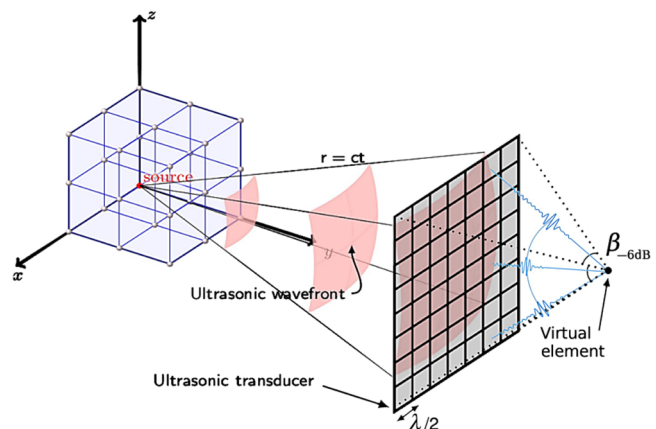
Fig. 1 The projection of acoustic wave emanated from a source within the FoV on the surface of a transducer. For every subelement, a delay is applied corresponding to the $\beta_{-6\,dB}$ diverging angle, to simulate the effect of negative focusing.

$$u_{\text{rec}}(x,y,z,t) = h_{\text{re}}^{\text{AIR}}(t) * h_{\text{re}}^{\text{SIR}}(x - x_{\text{re}}, y - y_{\text{re}}, z - z_{\text{re}}, t) * s. \tag{5}$$

Expanding the formula for every voxel within the aperture FOV yields a time-discrete matrix representation of the above formula.[34,35]

$$U_{\text{rec}} = M \cdot S, \tag{6}$$

where U is a vector containing concatenated time sampled recorded signals, ensemble of all of the recorded projections, $M_{J \times K}$ is the forward model (i.e., transfer matrix) describing the propagation of the K voxels (induced sources) to N detecting elements. For every voxel-element pair, there is an attributing impulse response of size L. The columns of M are containing the response of all elements for a given voxel, being vertically concatenated such that $J = L \times N$. The result is a convolution matrix that correlates a set of sources to a set of elements in the aperture.

$$M = \begin{bmatrix} h_{(1,1)}^{\text{IR}} & h_{(1,2)}^{\text{IR}} & \cdots & h_{(1,K)}^{\text{IR}} \\ h_{(2,1)}^{\text{IR}} & h_{(2,2)}^{\text{IR}} & \cdots & h_{(2,K)}^{\text{IR}} \\ \vdots & & \ddots & \vdots \\ h_{(N,1)}^{\text{IR}} & h_{(N,2)}^{\text{IR}} & \cdots & h_{(N,K)}^{\text{IR}} \end{bmatrix}_{J \times K}, \tag{7}$$

where $h_{(n,k)}^{\text{IR}} = h_{(n,k)}^{\text{AIR}} * h_{(n,k)}^{\text{SIR}}$. As for every voxel in the FoV, there is an attributed function, M can be treated as the matrix containing voxel expansion function. The integration over the spanned basis of each voxel implies the weighting value of the corresponding voxel and is proportional to the sensitivity of

transducers to that voxel. Accordingly, for the generic assessment of the imagining system, M is exploited by two evaluation methods, the voxel crosstalk matrix[28,36,37] and eigenanalysis.[26]

2.2 Voxel Crosstalk Matrix

The concept of crosstalk has been established in the assessment of system design, mainly to determine the reliability of the estimable coefficients.[38] The reliability in this context is the measure of strength and standalone contribution to individual sources. For a shift variant system such as OPUS, the coefficients are voxels energy. Hence, the effect of aperture in spatial blurring, aliasing, and spatial sensitivity is amenable to an analytic description. Voxel crosstalk matrix can be obtained as follows:

$$H = M^T M. \tag{8}$$

The crosstalk matrix H is essentially a square matrix with i'th diagonal elements (H_{ii}) describing the stand alone contribution of corresponding voxel {spatial sensitivity [Fig. 2(c)]} and off-diagonal elements, $H_{ij}; i \neq j$, representing the parasitic contribution of neighboring voxels, known as spatial aliasing. The value of $H_{ij}^2 / H_{ij} H_{ii}$ indicates the resolvability and consequently spatial aliasing between any two voxels. Therefore, a better imaging system is the one with weaker off-diagonal and stronger diagonal elements. The quantitative evaluation is possible through a set of metrics for systematic evaluation of the system voxel crosstalk matrix.[37] The utilized metrics in this context are the root mean square error (RMSE) and mean absolute error (MAE). These metrics are complementary to each other, providing a robust systematic approach in quantitative analysis of imaging performance. Together they render information about the variance and degree of error in a model.[39,40]
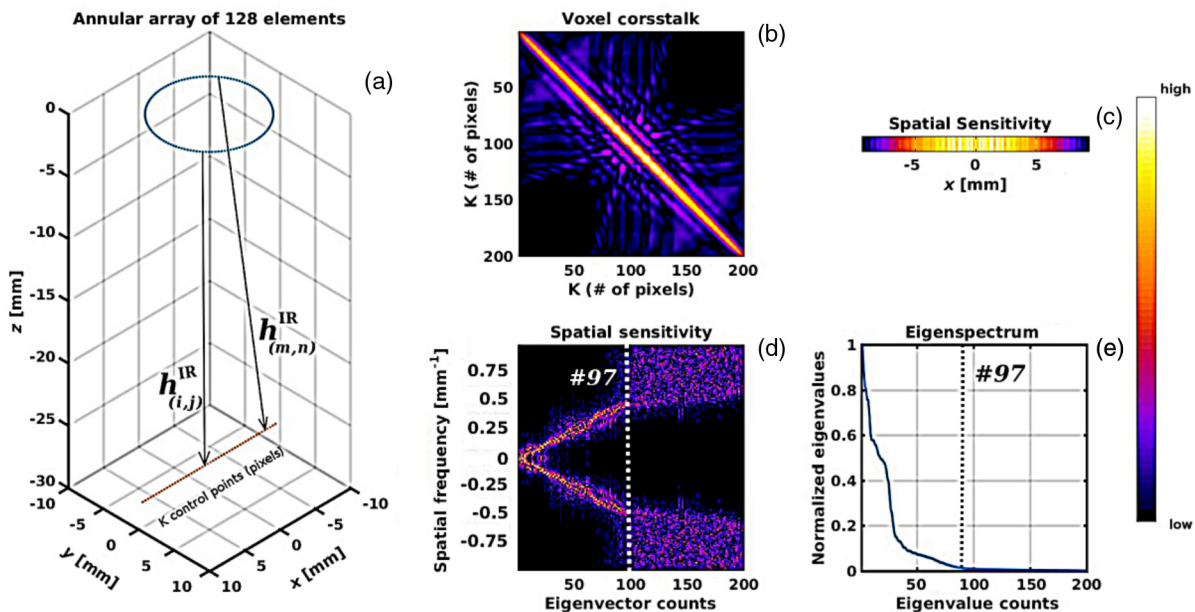
Fig. 2 (a) The transfer function h^{IR} correlates the pair of source-element for every 200 control points and 128 elements of annular array. (b) The corresponding voxel crosstalk matrix and (c) the spatial sensitivity of system obtained from the diagonal elements. (d) Spatial Fourier transform of eigenvectors of model matrix and (e) the eigenvalue distribution. For every eigenvector bound to a nonzero eigenvalue, there is a spatial frequency. The dashed line segregated the M_{prime} from M_{null}.

2.3 Eigenanalysis

As the name implies, eigendecomposition of the square matrix H features prominently the principal characteristics of the matrix by delivering the basis of eigenvectors q scaled by scalar eigenvalues λ.

$$Hq = \lambda q, \tag{9}$$

$$H = Q\Lambda Q^{-1}. \tag{10}$$

H is a Hermitian matrix with real and positive eigenvalues and linearly independent orthogonal eigenvectors q, Q (square matrix) is the projection of H in the eigenspace with eigenvectors along its columns, and Λ is a diagonal matrix containing eigenvalues λ_i along its diagonal such that $\lambda_1 > \lambda_2 > \cdots > \lambda_n$. The eigendecomposition can be considered as an expansion of the matrix with respect to its basis (i.e., eigenvectors), each with certain weighting coefficient (i.e., eigenvalues). Alternatively, eigenvectors of H can be calculated by singular value decomposition (SVD) of matrix M, given by $M = U\Sigma V$. From the mathematical point of view, $V = Q$ and Σ is a diagonal matrix containing singular values σ_i along its diagonal such that $\sigma_i = \sqrt{\lambda_i}$. Regardless, the matrix H can be represented simply as weighted and ordered combination of basis. The eigenvectors of the matrix H depict the principal structures of the detected wave components, reserving the original properties of the original matrix.[32]

Notably, the matrix M is a spatiotemporal matrix, therefore SVD decomposes M into the temporal matrix U and spatial matrix V. In other words, V is composing of K columns equal to the number of voxels while U is containing J columns equal to the number of recorded samples. Therefore, the frequency distribution of V has physical interpretation w.r.t. the sensitivity of system to certain spatial frequencies for the given voxels. This distribution would enable to extract the primary space M_{prime} (major components) from the null space M_{null} (e.g., noise).[26,41] In other words, distinguishing the strengths and deficiencies of these systems. The value of σ_i can be linked to the energy level or stability parameters of these components. In principle, the eigenvalues (or similarly singular values) are providing a measure of fidelity of these components such that the i'th eigenvalue exemplifies the i'th eigenvector's strength. In general, the most salient features of the matrix are stored in the first few eigenvectors (M_{prime}) where $\sigma_i > 0$. This boundary is referred to as the rank of matrix κ. Meanwhile, the sum of the eigenvalues or the nuclear norm of the matrix represents the energy of the matrix. Thus, the spectrum of eigenvalues, which is a generalized form of the Fourier power spectrum, allows discrimination between the primary and null space [Figs. 2(d) and 2(f)].

$$M = M_{\text{prim}} + M_{\text{null}}, \tag{11}$$

$$M_{\text{prim}} = \sum_{i=1}^{\kappa} \sigma_i u_i v_i^*, \tag{12}$$

$$\|(M - M_{\text{prim}})\|_2^2 = \sigma_{\kappa+1}^2. \tag{13}$$

The system with larger κ is imputed to the superior focusing competence[26] and more accurate set of acquired data. Eigenvalues with the associated eigenvectors are pointing out the maximum sensitivity of the system toward the direction of incoming wave, hence specifying the object features that are more accurately estimated. For a spatially variant system, this can be estimated by the Fourier of eigenvectors as well. Moreover, these vectors are containing the information about the missing projections, which implies the partial view angle [Fig. 2(d)] and resolvability of the spatial frequency component, hence redundancy of projections.

Subsequently, eigenanalysis estimates whether the formed image misses these angular frequencies, even if OPUS is an ideal reflection mode imaging system (i.e., infinite detectors). The quality and quantity of angular frequencies that an aperture can generate or similarly receive is contained in the model matrix [Fig. 2(d)]. Therefore, eigenanalysis provides a simple but credible mechanism for the comparative appraisal between two or more imaging systems.

2.4 Array Design

By taking into account the light delivery housing for perpendicular illumination, we are exploring the optimum geometrical properties for the OPUS handheld probe. The design array supposedly provides enough flexibility in elements' geometry and arrangement such that the periodicity is minimized and the agreement among directivity, sensitivity, and spatial aliasing can be settled. To begin with, segmented annular array of point-like transducers is considered. The elements are distributed equidistantly in a ring fashion around the optical probes, enabling real-time volumetric acquisition. The 11-mm ⊘ lumen is considered for the optical probe, which is in agreement with the limited 128 elements of 1λ width for the central frequency of 5 MHz with 80% fractional bandwidth.[23] Indeed, the transducer frequency response is of crucial importance and has a determinant role in the so called relative spatial resolution; defined as the ratio of the penetration limit to the depth resolution. The aforementioned frequency response would allow the detection of OA sources as deep as 38 mm *ex vivo* and 20 mm *in vivo*,[42,43] ideally down to the size of 0.3 mm.[44]

First, we explore the effect of element number, which has a reciprocal relationship to the interelement spacing. The optimization is pursued for the element size and geometrical distribution. The directive angular view (β) for the element edge a (height or width) is compensated by the negative focusing such that $\beta_{-6\,\text{dB}} = 2 \arcsin(0.6\lambda_c/a)$,[45] for λ_c is the wavelength corresponding to the central frequency. We simulated negative focusing for every element in the convex structure as if the focus is behind the transducer (Fig. 1). For the numerical calculation and *in silico* studies we found the well-known FieldII simulations toolbox[46] convenient.

3 Results

3.1 Voxel Crosstalk Matrix

Herein, the result of the voxel crosstalk analysis that estimates the spatial sensitivity and spatial aliasing for the given model matrix is presented. Figure 3 shows the effect of element number for four annular arrays composed of 32, 64, 128, and 256 point-like elements (0.5λ size) and an array of 128λ-width elements. Three axial slices within the FoV of $18 \times 18 \times 20$ mm^3 has been visualized, each composed of 100×100 voxels. The illustrated x-y planes are parallel to the surface of the aperture, at the depth of, respectively, 1, 2, and 3 cm away from the aperture

[Fig. 3(I)]. The spatial aliasing for the most and least sensitive voxels in the FoV is provided in Fig. 3(II). Presented in Fig. 3 (III), the two metrics of RMSE and MAE are negatively oriented scores and their parallel variation in the same order suggests the existence of many small errors. The variance of the errors is corresponding to the absolute difference between the values of two metrics.[39] The qualitative and quantitative analyses indicate the improvement in sensitivity and aliasing with the increase in transducer counts. However, for the case where the overall active area is the same, the aperture with larger elements showcases a better performance.

Figure 4 presents the results of voxel crosstalk analysis w.r.t. the height of the transducers while the interelement spacing is limited to λ. The larger elements give rise to higher sensitivity and lesser spatial aliasing. More voxels are contributing to the parasitic signals but in lesser values, which also means lesser sidelobe value. The quantitative analysis confirms the qualitative interpretation [Fig. 4(III)]. As the size of element increases, the values of both metrics decrease but the difference between them increases. Due to its point-like transducers, the aperture with 0.5λ element's height[22] is exempt and here is set as the reference for quantitative analysis.
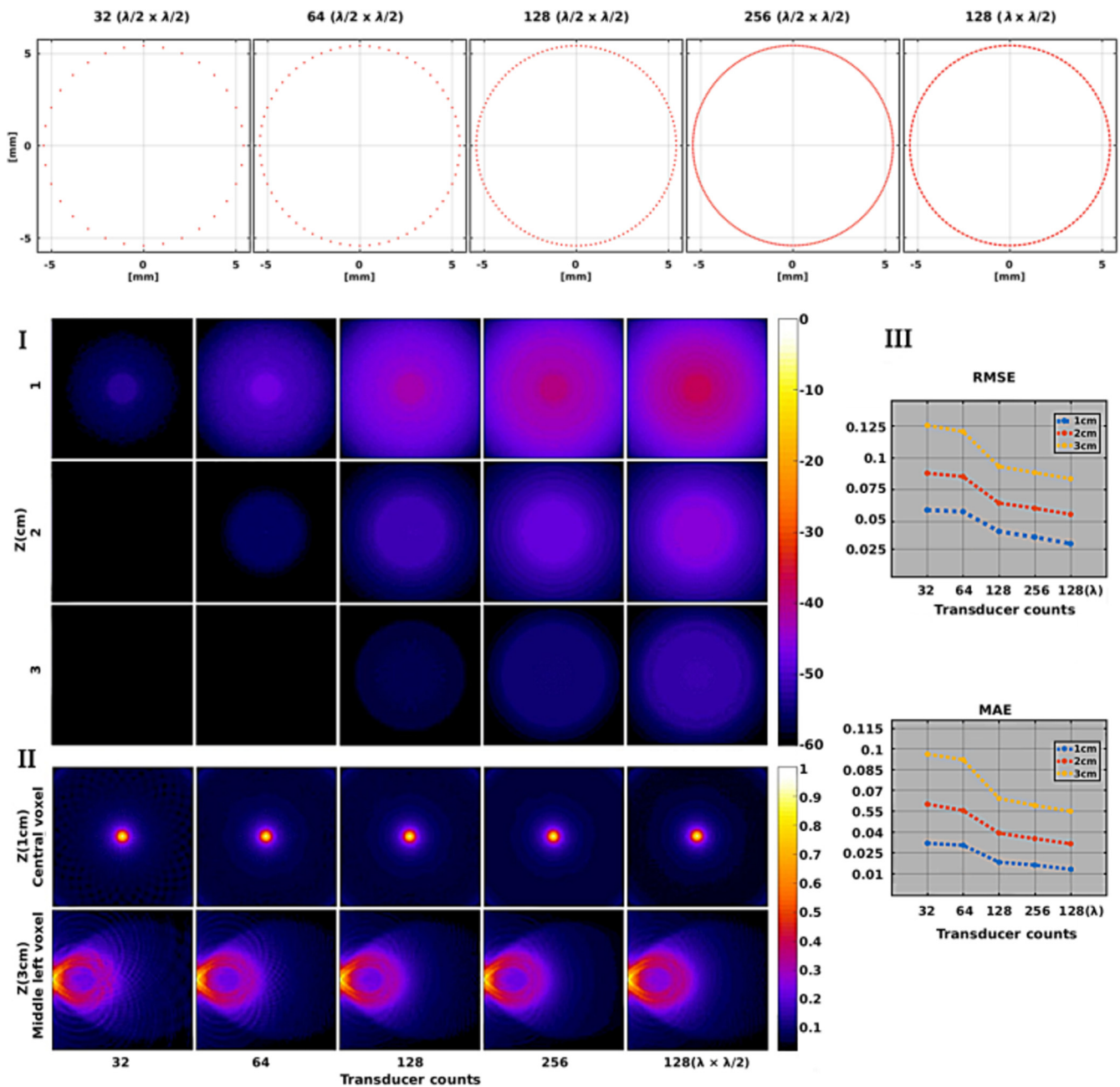
Fig. 3 Crosstalk analysis on the effect of element number for segmented annular array. I: 60 dB logarithmic scale (w.r.t. the pressure at the surface of transducers) spatial sensitivity. II: Parasitic contribution to the central voxels of the plane at $z = 1$ cm (upper row) and marginal voxels (lower row) of the plane at $z = 3$ cm. III: Quantitative metrics.
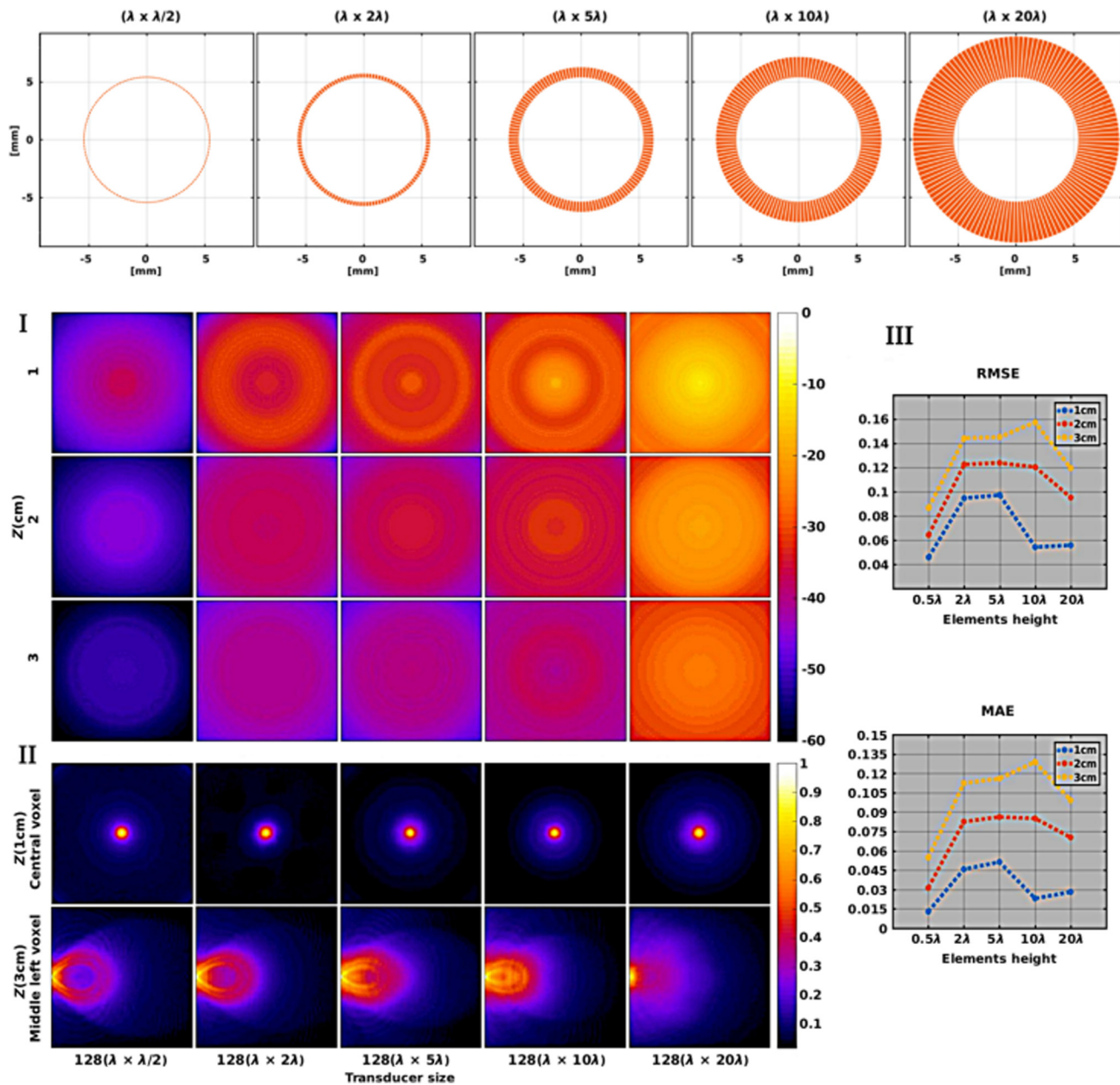
Fig. 4 Crosstalk analysis on the effect of element height for segmented annular array. I: 60 dB logarithmic scale spatial sensitivity. II: Parasitic contribution to the central voxel of the plane at $z = 1$ cm (upper row) and marginal voxel (lower row) of the plane at $z = 3$ cm. III: Quantitative metrics.

In pursuit of an aperture with lesser periodicity[5,18] (i.e., aliasing), Fig. 5 compares the result of voxel crosstalk analysis for three virtual apertures with rather same element size but different arrangements. The performance of segmented annular array of $1\lambda \times 20\lambda$ element size is shown alongside the annular circular array and annular spiral array of $5\lambda \times 5\lambda$ element size [Fig. 5(IV)]. For the last two, the uniform distribution of energy over the FoV is expected due to the rather sparser geometry. Yet, the lack of uniform overlap among the elements' view angle costs the energy in the central area, shown in Fig. 5(I). Figure 5(III) outlines the quantitative analysis for the three apertures. The segmented annular array showcases lesser errors and lesser difference between RMSE and MAE, an indication for lesser variance in the error.[39]

3.2 Eigenanalysis

In this section, we summarize the effect of aperture partial view on the information loss, using eigenanalysis. The system comparison depends both on the number of effective components and the structure of the singular vectors. As the arrays are circularly symmetrical, we speculate the variations over four 18 mm lines of 200 control points at four different depths. The control points lie on a plane parallel to the aperture. Figure 6 shows the spatial Fourier transform of the right-hand side singular vectors, for four axial planes away from the surface of aperture, respectively, at 1, 10, 20, and 30 mm.

In general, there are less available spectral components with the depth (columns), recalling that OPUS is a spatially variant
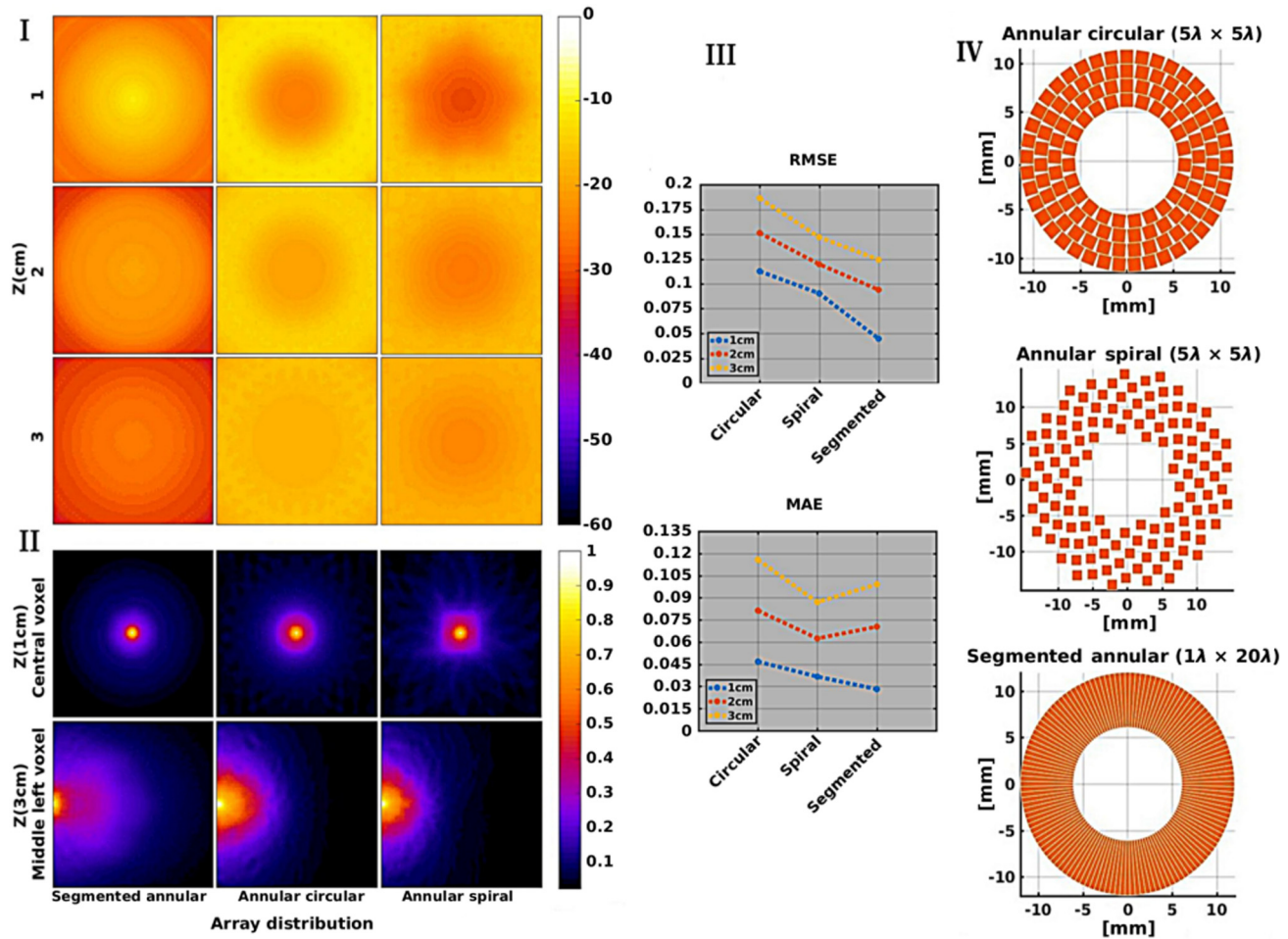
Fig. 5 Qualitative and quantitative interpretation of crosstalk analysis on the effect of elements arrangement. I: 60 dB logarithmic scale spatial sensitivity. II: Parasitic contribution to the central voxel of the plane at $z = 1$ cm (upper row) and marginal voxel (lower row) of the plane at $z = 3$ cm. III: Quantitative metrics. IV: Array geometries.

imaging system. For the case where the object plane is near the aperture (first row of Fig. 6), the lower spatial frequencies are associated with discrepancies due to the limited directivity of large elements (the left side of the first white-dashed line). On the other side, the higher frequency components in the right side of the second dashed line are not containing information but noise. The rather meaningful information is limited to the area between the two dashed lines, thus less sensitivity to generated OA clutters.[47] For the other planes, where the control points are farther from the aperture, the lower angular frequency components are stronger and contain resolvable structures. The separating border between the noise and meaningful data is highlighted by the white-dashed line. The adjacent number is pinpointing the turning point of which segregates the resolvable and unresolvable spectral information. One can notice that for the segmented annular array, the larger element, hence the larger aperture is accompanied by more and finer definition of the frequency components where each meaningful singular vector is associated with narrower spectrum.

By analogy to the segmented annular array, both annular circular and annular spiral arrays are containing more robust DC components for the axial planes in the far-field (≥ 1 cm). However, the number of valuable components (marked next to the dashed line) remains comparative. In addition, the rippled arms of annular circular and annular spiral arrays are indicating

less resolvability for the frequency components and more aliasing. This is not observed in the segmented annular array where the thinner arms are implying a better resolvability for frequency components. Therefore, the imaging performance of segmented annular array can outperform the other layouts, for both OA and ultrasound imaging.

4 Discussion and Conclusions

This study has detailed the theory of a framework in which the efficiency of a generic assessment tool in evaluating the performance of array imaging was demonstrated. The main focus of this work was design and characterization of a high compelling volumetric handheld probe for OPUS imaging. On that note, several substantial steps have been taken.

An underpinning step of this work was deriving a discrete linear model that explains the imaging performance of the designed system. The calculation is based on the system impulse response that correlates the sources to the recorded signals via the model matrix of the aperture. The purpose of developing the model was mainly to characterize and further optimize the imaging aptitude of the array as a spatially variant limited view imaging system. It is worth noting that the same model can be employed in conjunction with image reconstruction as an accurate imaging operator.
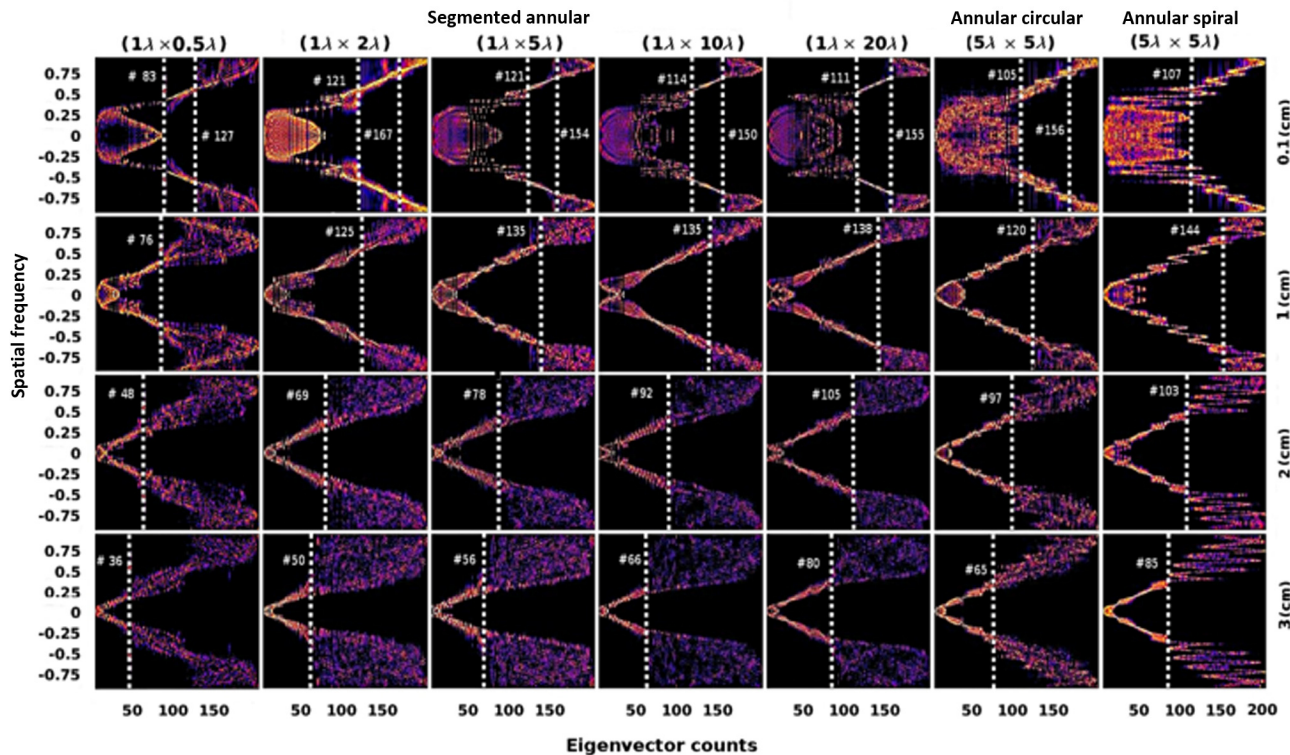
Fig. 6 The spatial Fourier transform of eigenvectors of the model matrix for 200 control points along the central line at four different axial planes. The white-dashed line indicates the borderline between the M_{prime} and M_{null}.

A fruitful comparison assessment tool that fully investigates the dynamics of the imaging device and allows for optimization w.r.t. the imaging performance has been followed. In particular, the effect of number, size, and geometrical location of the elements and their optimum configurations was considered. By employing the spatial crosstalk, potentially a principled argument is provided for comparative studies among the performances of different imaging systems. On the other hand, the eigenanalysis is providing an argument w.r.t. partial view angle. Together they enable to draw a valid conclusion about imaging performance of the imaging system.

Finally, the avails of the annular probes in the OPUS imaging by elaborating the appraisal analysis were demonstrated. Throughout the analysis, it was found that the annular geometry provides a unique layout for moderately large aperture containing limited number of elements. In addition, the central cavity preserves the housing for in-line arrangement between the optical source and transducers. Owing to its circular symmetry and inherent lumen, uniform excitation/insonification within the FoV is achievable [Fig. 4(I)], which is suitable for volumetric imaging. These studies confirmed that the superior performance is accompanied by increasing the number and size of the elements as long as the directivity is compensated. The latter can take place by the help of negative focusing via either of convex transducer or negative lens. It was shown that for these elements, the least aliasing does not necessarily correspond to the aperture with periodicity. Overall, the performance of segmented annular array in imaging outweighs the rest of geometries, considering the resolution, detectability, and uniform response for both modalities. For the sake of simplicity, we only considered flash-echo mode for US imaging. However, the approach can be extended to more sophisticated beamforming algorithms where the projections and therefore contrast and resolution are increased. One future research line is the objective assessment of the evaluated arrays based on the final image quality. However, the risk of bias evaluation with respect to the merits of reconstruction algorithm remains.

In conclusion, this work presents the development of a multi-purpose handheld probe for volumetric OA ultrasound imaging. The theory behind this development has been established, and the dynamics of a new geometry for volumetric OPUS imaging has been assessed. Last but not least, we restricted our analysis to the geometrical properties of the array. Further optimization w.r.t. the transducing properties is deferred to future research.

Disclosures

The authors have no conflicts of interest to declare.

References

1. P. N. T. Wells, *Scientific Basis of Medical Imaging*, Churchill Livingstone, Edinburgh (1982).

2. P. J. van den Berg, K. Daoudi, and W. Steenbergen, "Pulsed photoacoustic flow imaging with a handheld system," *J. Biomed. Opt.* **21**(2), 026004 (2016).

3. Y. Wang et al., "In vivo three-dimensional photoacoustic imaging based on a clinical matrix array ultrasound probe," *J. Biomed. Opt.* **17**(6), 061208 (2012).

4. M. Gerling et al., "Real-time assessment of tissue hypoxia in vivo with combined photoacoustics and high-frequency ultrasound," *Theranostics* **4**(6), 604–613 (2014).

5. A. Ramalli et al., "Density-tapered spiral arrays for ultrasound 3-D imaging," *IEEE Trans. Ultrason. Ferroelectr. Freq. Control* **62**(8), 1580–1588 (2015).

6. G. Paltauf, R. Nuster, and P. Burgholzer, "Weight factors for limited angle photoacoustic tomography," *Phys. Med. Biol.* **54**(11), 3303–3314 (2009).

7. E. Mercep et al., "Hybrid optoacoustic tomography and pulse-echo ultrasonography using concave arrays," *IEEE Trans. Ultrason. Ferroelectr. Freq. Control* **62**(9), 1651–1661 (2015).

8. J. Gateau et al., "Improving visibility in photoacoustic imaging using dynamic speckle illumination," *Opt. Lett.* **38**(23), 5188–5191 (2013).

9. L. Wang et al., "Ultrasonic-heating-encoded photoacoustic tomography with virtually augmented detection view," *Optica* **2**(4), 307–312 (2015).

10. R. Ellwood et al., "Photoacoustic imaging using acoustic reflectors to enhance planar arrays," *J. Biomed. Opt.* **19**(12), 126012 (2014).

11. B. Huang et al., "Improving limited-view photoacoustic tomography with an acoustic reflector," *J. Biomed. Opt.* **18**(11), 110505 (2013).

12. J. A. Jensen et al., "Sarus: a synthetic aperture real-time ultrasound system," *IEEE Trans. Ultrason. Ferroelectr. Freq. Control* **60**(9), 1838–1852 (2013).

13. G. R. Lockwood et al., "Optimizing the radiation pattern of sparse periodic linear arrays," *IEEE Trans. Ultrason. Ferroelectr. Freq. Control* **43**(1), 7–14 (1996).

14. A. Austeng and S. Holm, "Sparse 2-D arrays for 3-D phased array imaging-design methods," *IEEE Trans. Ultrason. Ferroelectr. Freq. Control* **49**(8), 1073–1086 (2002).

15. J. T. Yen, J. P. Steinberg, and S. W. Smith, "Sparse 2-D array design for real time rectilinear volumetric imaging," *IEEE Trans. Ultrason. Ferroelectr. Freq. Control* **47**(1), 93–110 (2000).

16. M. Karaman et al., "Minimally redundant 2-D array designs for 3-D medical ultrasound imaging," *IEEE Trans. Med. Imaging* **28**(7), 1051–1061 (2009).

17. J. W. Choe et al., "Real-time volumetric imaging system for CMUT arrays," in *IEEE Int. Ultrasonics Symp. (IUS)*, pp. 1064–1067, IEEE (2011).

18. O. Martínez-Graullera et al., "2D array design based on fermat spiral for ultrasound imaging," *Ultrasonics* **50**(2), 280–289 (2010).

19. E. Roux et al., "2-D ultrasound sparse arrays multidepth radiation optimization using simulated annealing and spiral-array inspired energy functions," *IEEE Trans. Ultrason. Ferroelectr. Freq. Control* **63**(12), 2138–2149 (2016).

20. X. L. Deán-Ben and D. Razansky, "Portable spherical array probe for volumetric real-time optoacoustic imaging at centimeter-scale depths," *Opt. Express* **21**(23), 28062–28071 (2013).

21. T. F. Fehm, X. L. Deán-Ben, and D. Razansky, "Four dimensional hybrid ultrasound and optoacoustic imaging via passive element optical excitation in a hand-held probe," *Appl. Phys. Lett.* **105**(17), 173505 (2014).

22. S. J. Norton, "Synthetic aperture imaging with arrays of arbitrary shape. II. The annular array," *IEEE Trans. Ultrason. Ferroelectr. Freq. Control* **49**(4), 404–408 (2002).

23. M. A. Kalkhoran et al., "Volumetric pulse echo and optoacoustic imaging by elaborating a weighted synthetic aperture technique," in *IEEE Int. Ultrasonics Symp. (IUS)*, pp. 1–4, IEEE (2015).

24. M. A. Kalkhoran, F. Varray, and D. Vray, "Dual frequency band annular probe for volumetric pulse-echo optoacoustic imaging," *Phys. Proc.* **70**, 1104–1108 (2015).

25. M. Pramanik, G. Ku, and L. V. Wang, "Tangential resolution improvement in thermoacoustic and photoacoustic tomography using a negative acoustic lens," *J. Biomed. Opt.* **14**(2), 024028 (2009).

26. M. Tanter et al., "Optimal focusing by spatio-temporal inverse filter. I. Basic principles," *J. Acoust. Soc. Am.* **110**(1), 37–47 (2001).

27. R. J. Zemp, C. K. Abbey, and M. F. Insana, "Linear system models for ultrasonic imaging: application to signal statistics," *IEEE Trans. Ultrason. Ferroelectr. Freq. Control* **50**(6), 642–654 (2003).

28. M. Roumeliotis et al., "Analysis of a photoacoustic imaging system by the crosstalk matrix and singular value decomposition," *Opt. Express* **18**(11), 11406–11417 (2010).

29. P. R. Stepanishen, "Transient radiation from pistons in an infinite planar baffle," *J. Acoust. Soc. Am.* **49**(5B), 1629–1638 (1971).

30. Z. Wang, S. Ha, and K. Kim, "A new design of light illumination scheme for deep tissue photoacoustic imaging," *Opt. Express* **20**(20), 22649–22659 (2012).

31. P. M. Morse and K. U. Ingard, *Theoretical Acoustics*, Princeton university press, Princeton, New Jersey (1968).

32. C. Prada et al., "Decomposition of the time reversal operator: detection and selective focusing on two scatterers," *J. Acoust. Soc. Am.* **99**(4), 2067–2076 (1996).

33. A. Lhémery, "Impulse-response method to predict echo-responses from targets of complex geometry. Part I: theory," *J. Acoust. Soc. Am.* **90**(5), 2799–2807 (1991).

34. F. Lingvall and T. Olofsson, "On time-domain model-based ultrasonic array imaging," *IEEE Trans. Ultrason. Ferroelectr. Freq. Control* **54**(8), 1623–1633 (2007).

35. M.-L. Li, Y.-C. Tseng, and C.-C. Cheng, "Model-based correction of finite aperture effect in photoacoustic tomography," *Opt. Express* **18**(25), 26285–26292 (2010).

36. J. Qi and R. H. Huesman, "Wavelet crosstalk matrix and its application to assessment of shift-variant imaging systems," *IEEE Trans. Nucl. Sci.* **51**(1), 123–129 (2004).

37. P. Wong et al., "Objective assessment and design improvement of a staring, sparse transducer array by the spatial crosstalk matrix for 3d photoacoustic tomography," *PLoS One* **10**(4), e0124759 (2015).

38. H. H. Barrett et al., "Objective assessment of image quality. II. Fisher information, Fourier crosstalk, and figures of merit for task performance," *J. Opt. Soc. Am. A* **12**(5), 834–852 (1995).

39. C. J. Willmott and K. Matsuura, "Advantages of the mean absolute error (MAE) over the root mean square error (RMSE) in assessing average model performance," *Clim. Res.* **30**(1), 79–82 (2005).

40. T. Chai and R. R. Draxler, "Root mean square error (RMSE) or mean absolute error (MAE)?–arguments against avoiding RMSE in the literature," *Geosci. Model Dev.* **7**(3), 1247–1250 (2014).

41. T. M. Rossi and I. M. Warner, "Rank estimation of emission excitation matrixes using frequency analysis of eigenvectors," *Anal. Chem.* **58**(4), 810–815 (1986).

42. K. Song and L. V. Wang, "Deep reflection-mode photoacoustic imaging of biological tissue," *J. Biomed. Opt.* **12**(6), 060503 (2007).

43. L. V. Wang, "Multiscale photoacoustic microscopy and computed tomography," *Nat. Photonics* **3**(9), 503–509 (2009).

44. V. G. Andreev, A. A. Karabutov, and A. A. Oraevsky, "Detection of ultrawide-band ultrasound pulses in optoacoustic tomography," *IEEE Trans. Ultrason. Ferroelectr. Freq. Control* **50**(10), 1383–1390 (2003).

45. B. Woodward, S. Hole, and W. Forsythe, "Transducer design for a correlation log," *Ultrasonics* **31**(1), 21–34 (1993).

46. J. A. Jensen, "Field: a program for simulating ultrasound systems," in *10th Nordicbaltic Conf. on Biomedical Imaging*, **Vol. 4**, pp. 351–353, Citeseer (1996).

47. M. Jaeger, J. C. Bamber, and M. Frenz, "Clutter elimination for deep clinical optoacoustic imaging using localised vibration tagging (LOVIT)," *Photoacoustics* **1**(2), 19–29 (2013).

Mohammad Azizian Kalkhoran graduated from Heidelberg University, Germany, in 2013. Currently, he is a PhD student at Creatis Laboratory at INSA Lyon. His current research interests include hybridized optoacoustic and ultrasound, optical microscopy, and tomography and fluorescent imaging.

Didier Vray is currently a professor of Signal Processing and Computer Sciences at INSA-Lyon, France. Since he joined the research laboratory CREATIS, his main research interest has focused on ultrasound medical imaging. His research includes vascular imaging, flow imaging, tissue motion estimation, and bimodality US/optics imaging. He is the author of more than 100 scientific publications and 2 issued patents in this field.